POLITECNICO DI TORINO
Repository ISTITUZIONALE

Investment casting of porous Mg-alloy networks biomechanically tuned for bone implant applications

Original
Investment casting of porous Mg-alloy networks biomechanically tuned for bone implant applications / Dmitruk1, A., Andrés Díaz Lantada, ·., Ferraris, S., Natalia obaczRany, ·., Spriano, S., Krzysztof Naplocha, ·.. - In: THE INTERNATIONAL JOURNAL OF ADVANCED MANUFACTURING TECHNOLOGY. - ISSN 1433-3015. - 135:(2024), pp. 3473-3486. [10.1007/s00170-024-14658-6]

Availability:
This version is available at: 11583/2995459 since: 2024-12-16T16:46:39Z

Publisher:
Springer

Published
DOI:10.1007/s00170-024-14658-6

Terms of use:

This article is made available under terms and conditions as specified in the corresponding bibliographic description in the repository

Publisher copyright

(Article begins on next page)

07 November 2026

The International Journal of Advanced Manufacturing Technology (2024) 135:3473–3486
https://doi.org/10.1007/s00170-024-14658-6

ORIGINAL ARTICLE

Investment casting of porous Mg-alloy networks biomechanically tuned for bone implant applications

Anna Dmitruk[1] · Andrés Díaz Lantada[2] · Sara Ferraris[3] · Natalia Łobacz-Raźny[1] · Silvia Spriano[3] · Krzysztof Naplocha[1]

Received: 22 June 2024 / Accepted: 9 October 2024 / Published online: 29 October 2024
© The Author(s) 2024

Abstract
Manufacturing technology has been refined and described for the fabrication of honeycomb-based bioresorbable networks for temporal bone replacement applications. Two novel techniques, digital light processing and investment casting, were utilized to produce customized, shape-optimized cellular constructs with additional orifices promoting tissue ingrowth during osteo-regeneration. For this purpose, a conventional magnesium casting alloy (AZ91) was chosen. Numerical simulations were conducted to predict the compressive behavior of the proposed biodegradable lightweight scaffolds. Spatial castings were adjusted to possess mechanical properties comparable to the ones of cortical or trabecular bones. Two kinds of protective coatings (plasma electrolytic oxidation and organic ones based on natural polyphenols from tea extract) were deposited and characterized. They can be utilized to control the degradation rate during exploitation to achieve a predictable implant lifespan. The elaborated layers aim to mitigate the rapid corrosion of magnesium substrates by prolonging their bioresorption time and thus expanding their applicability in osseointegration. To evaluate this assumption, immersion tests in phosphate-buffered saline were performed, showing better chemical resistance of PEO coating and as-cast sample (for both mass gain by below 1%), and visible increase in mass of sample coated with organic coating (increase by almost 5%). Compressive strength results from numerical approach were further validated by experimental compression tests, showing that PEO coating deteriorated compressive strength by almost 3%, and organic coating improved it by over 9%. Results achieved in numerical approach were better than expected for stiffer sample, and slightly lower for the one with bigger pores.

Keywords Investment casting · Cellular magnesium structure · Bone implant · Plasma electrolytic oxidation · Organic coating · Compressive behavior

1 Introduction

Lightweight design typically leads to porous structures or lattices and plays a fundamental role in modern sustainable structural design [1, 2]. Traditional manufacturing processes such as casting [3], foaming [4, 5], molding with porogens [6], or soldering [7], among others, coexist with alternatives derived from the introduction of additive manufacturing technologies (AMTs) [8, 9]. The latter herald the dream of total design freedom, but have some important drawbacks derived from the limited portfolio of processable materials, the need for supporting structures in several AM processes, the typically slow production speed, the intrinsic anisotropy of the additive approach, the achievable part sizes, or the final surface quality, to cite a few challenging aspects of AMTs. It is therefore necessary for further research in straightforward design and manufacturing methods for lightweight structures that may combine the benefits from traditional and additive strategies, as some researchers have explored additive manufacturing-assisted investment casting and rapid investment casting [10, 11], which has led to enhanced design versatility and mechanical properties.

These lightweight structures are important in aeronautics and space vehicles [12, 13], in innovative machine elements and chassis [14], in robotics and automation chains [15, 16], and in many other structural applications [1,

✉ Anna Dmitruk
anna.dmitruk@pwr.edu.pl

[1] Department of Lightweight Elements Engineering, Foundry and Automation, Wroclaw University of Science and Technology, Wrocław, Poland

[2] Mechanical Engineering Department, Universidad Politécnica de Madrid, Madrid, Spain

[3] Department of Applied Science and Technology, Politecnico Di Torino, Turin, Italy

2]. Among them, those linked to the biomedical field are probably the most promising in terms of societal impacts, as bioinspired design methods for improved biomechanics are directly connected to lightweight structures, in which functionally graded lattices or regions with varied pore sizes are becoming the main trend [17, 18]. Indeed, biomedical research fields like tissue engineering or bio-fabrication profoundly rely on the use of porous scaffolding lattices or lightweight structures that provide cells with an implantable artificial extracellular matrix [19, 20]. These advanced implants are currently researched as one of the most promising repair and regeneration strategies.

Several combinations of materials and processes have been explored with the aim of innovating implants and developing the ideal tissue engineering scaffolds [21, 22]. As regards the potential for bone repair, magnesium is becoming a popular research option for next-generation implants and scaffolds and is already generating great expectations due to its recently reported osteoconductivity, anti-bacterial properties, biodegradability, and biomechanical performance [23–26]. Design-controlled porous Mg structures and tissue engineering scaffolds have been recently obtained employing different additive manufacturing procedures, such as laser powder bed fusion, wire-arc additive manufacturing, paste extrusion, and jetting technologies [27–30]. However, AM processes can lead, in some cases, to high levels of porosity, which affects structural integrity and control upon biodegradation. However, creating large-sized and fully dense Mg structures by additive manufacturing remains a challenge [27].

In this study, an alternative hybrid strategy is proposed and exemplified by the manufacturing of two different porous Mg-alloy (AZ91) networks, one with mechanical properties adjusted to those from the cortical bone, and one fine-tuned to the characteristics of trabecular bone. The complete design, simulation, manufacturing, and testing procedures for these porous Mg-based scaffolds are presented and methodically compared with those from achievable employing alternative or complementary approaches, in terms of biomechanical performance, structural integrity, manufacturability, and environmental impacts. Additive manufacturing and subsequent investment casting innovative techniques are employed to manufacture customized cellular constructs based on honeycombs with multiple orifices promoting bone tissue ingrowth and tailoring castings' mechanical properties. Evaluation of compressive behavior was performed by comparative analysis of the numerical simulation and experimental results. Moreover, two kinds of protective coatings aiming to control the degradation rate of the implants were deposited and preliminarily characterized. Their efficacy was assessed after immersion tests in phosphate buffered saline (PBS) for 6 h.

2 Materials and methods

The experiment flow is shown in Fig. 1. Specimens were fabricated by two joint techniques: 3D printing (digital light processing, DLP) and subsequent investment castings. Models were firstly designed in Autodesk Inventor Professional 2019 software and then transferred into G-code files with the use of Lychee Slicer. Honeycomb patterns were created in two types: (a) smaller cells (3.5 mm diagonally, designated as HEX 3.5) with wall perforations of Φ1.5 mm; (b) bigger cells (6 mm diagonally, designated as HEX 6) with orifices of 3 mm (see Fig. 1). A constant wall thickness of 0.6 mm was applied for all of the samples. Honeycomb cores were peripherally enveloped with outer tubes of the same thickness.

During computational modeling, Autodesk inventor.ipt extension files with the designed lattices were imported with NX-12 (Siemens Product Lifecycle Management Solutions) for performing finite element simulations, predicting their mechanical performance, and verifying the use of computational modeling for experimental planning and optimization purposes. In short, preprocessing involved geometrical discretization, application of Mg alloy from the available materials library and definition of loads and boundary conditions to simulate compression testing of the material. "NX Simcenter Nastran structural" solver and a linear static solution (SOL103) were chosen for these studies. Meshing was performed using tetrahedral elements and an initial sensitivity analysis was carried out by employing two different form functions (4-node and 10-node tetrahedrons) and two different mesh sizes, starting from the automatically advised size by NX-12 and employing at least two elements across the thickness. No relevant differences were detected in the various simulations of the sensitivity analysis, and a mesh size of 0.25 mm was finally employed. The bottom surfaces of the geometries under study (HEX 3.5 and HEX 6 with the reinforcement outer tubular structures) were fixed and a set of compression loads (100 N, 1000 N and 5000 N) along -Z axis were applied to the upper surfaces. After solving, post-processing allowed results visualization and critical analysis, as further explained in the results and discussion section.

Spatial constructs were printed from Bluecast X5 photocurable resin with the use of an Anycubic Photon Mono X printer. After this process, they were subjected to further cleaning and additional curing with Anycubic Wash & Cure Plus equipment. In the next step plaster molds (Ransom & Randolph Argentum) were prepared on their basis, after attaching of the wax gating systems to the prints. Afterwards, when the gypsum initially solidified, molds were subjected to heat treatment during the burn-out cycle

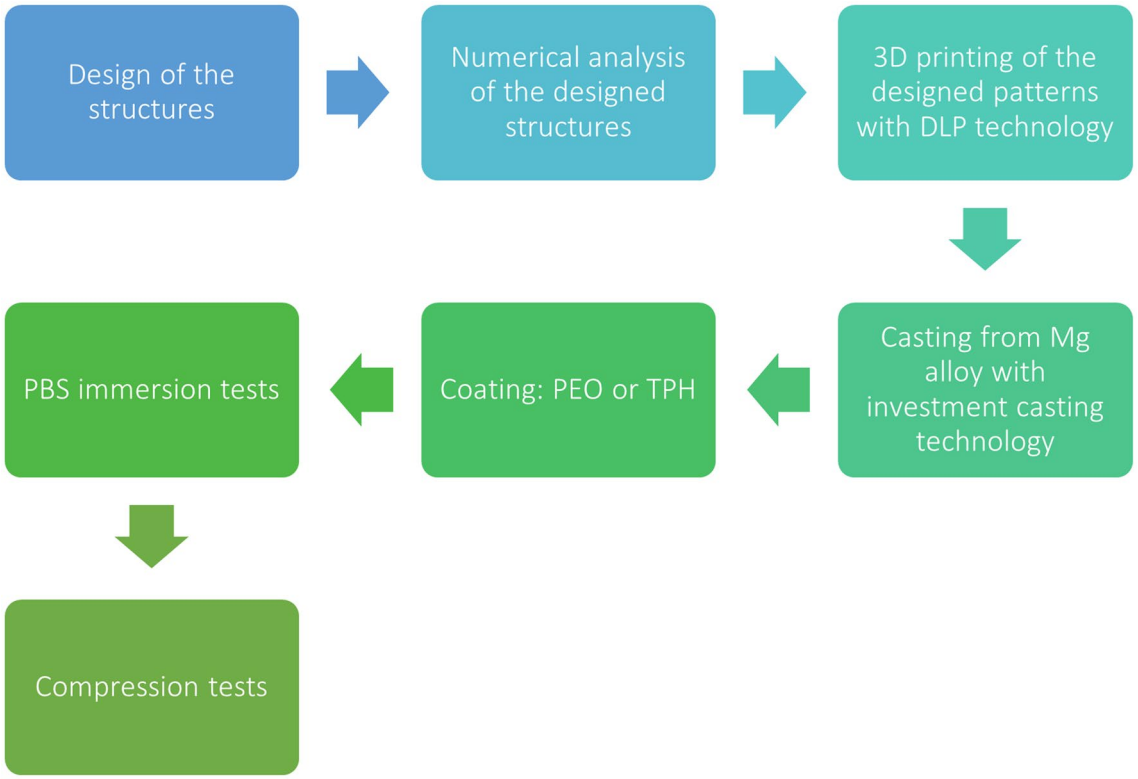

Fig. 1 The flowchart of the experiment

with a maximum temperature of 730 °C. During this process, the plaster went through dehydration and hardening phases and the polymer and wax model was removed from the mold's cavity by complete gasification. A preheated mold was filled with the chosen magnesium casting alloy – AZ91 with the chemical composition of 9 wt.% Al, 0.13 wt.% Mn, and 0.7 wt.% Zn, the remainder Mg. Metal heated up to a temperature of 730 °C was poured under low pressure into the molds to reflect the shape of the patterns. In order to limit any undesirable exothermic reactions of liquid magnesium alloy with oxygen, a protective atmosphere of SF6 was applied. Nevertheless, as this alloy is prone to react with the molding material as well, their interaction had to be shortened by accelerating the cooling stage. Finally, samples were washed and cleaned from the remnants of the gypsum mass. SEM observations were done by means of a Hitachi TM3000 scanning electron microscope with EDS/EDX analyzer.

Before PEO treatment, all samples were cleaned with acetone in an ultrasonic cleaner for 10 min, then immersed in distilled water and dried at room temperature. Power supply used in the experiment was produced by Mic-Arc S.C, Poland. The PEO process was performed in an alkaline solution based on 12 g/L $Na_3PO_4 \cdot 12H_2O$ and 1 g/L KOH. As an anode, a metal container filled with electrolyte was used. A mechanical stirrer was employed to keep the electrolyte moving during the process. The container with the electrolyte was immersed in a water bath connected to a chiller to cool down the electrolyte during the process, and the temperature was maintained at approx. 15 °C. Samples were mounted on aluminum rods and treated for 15 min. The voltage limit was set to 600 V, while current density was set to 0.1 A/cm^2. After the treatment, samples were immersed in water and dried at room temperature. Average process parameters applied and registered during coating are given in Table 1. The differences in voltage values between sample treatments might be connected to a different surface area; possible porosities of the castings and ceramic residues present inside them.

Some samples were coated with a thin organic layer to modulate the degradation kinetics. An extract of tea was used for this purpose; the extraction from green tea leaves was described in [31, 32]. A 30 mg/ml water solution of

Table 1 Parameters of PEO process

Sample	Frequency (Hz) – pulse on:off (ms)	Maximal voltage/final voltage (V)
PEO-coated HEX 3.5	1000—0.3:0.7	600/414
PEO-coated HEX 6	1000—0.3:0.7	600/364

the tea extract (TPH) was used for the coating. Mg porous samples were sandblasted with electrocorundum and then washed for 5 min in ethanol in an ultrasonic bath, subsequently rapidly rinsed in ultrapure water, and dried with compressed air. Washed samples were then soaked in the TPH solution in an orbital shaker for 10 min at 37 °C and 120 rpm (KS 4000i control, IKA), washed in ethanol for 5 min in an ultrasonic bath, rinsed with ultrapure water, and dried at 37 °C in an incubator. These samples will be known as TPH-coated HEX from now on. To verify the presence of the organic layer and investigate its morphology, the samples were analyzed by means of Field Emission Scanning Electron Microscopy (FESEM, SUPRATM 40, Zeiss). The effectiveness of the deposited layers in terms of controlling the degradation rate was appraised by immersion tests in PBS (PBS tablets without Calcium and Magnesium, MP Biomedicals) for 6 h. Measurements of mass gain and the pH of the solution were carried out hourly. Each time cast samples were taken out of the PBS, they were washed with distilled water and subsequently dried with hot air.

Compression strength tests at 2 mm/min were performed with the use of a Tinius Olsen H25KT testing machine equipped with a 25 kN maximum load.

3 Results and discussion

3.1 Outcomes of numerical simulation

The results of the linear simulation of static loading for both types of the analyzed structures, with incorporated tubular reinforcements, are shown in Table 2 for the three loads considered: 100, 1000, and 5000 N. The resulting stress and strain distributions obtained with the use of the Von Mises hypothesis for the highest load are shown in Fig. 2. The apparent Young's compression moduli were calculated for the porous structures considering the applied loads and the dimensions of the circumscribed cylinder to the porous structures, which has an initial length of 30 mm and a diameter of approx. 20 mm. Predicted values of the apparent Young's modulus (7–11 GPa) are suitable for the planned application in the bone implants sector [33–36]. In fact, depending on pore size and geometry the stiffness of the structures can be fine-tuned: HEX 6 would be closer to the desired values for trabecular bone and HEX 3.5 would be closer to those from cortical regions. Combinations of these kinds of cells, adequately assigned to different regions of an implant, would lead to biomimetic functional gradients of mechanical properties, which constitutes an interesting research direction for the future. Total displacement up to a load of 5000 N is rather negligible (up to 44 µm for the stiffer structure with smaller cells and up to 70 µm for the other one). Moreover, the calculated maximum stresses for these constructs are respectively equal to 172 and 283 MPa. Due to the openings incorporated within the honeycomb cores, the stress accumulation takes place directly alongside their edges. These areas are presumed to work as buckling initiators when the load is further increased. In the simulations with higher mechanical loads of 5000 N, (shown in Fig. 1c–j, as representative examples of simulations summarized in Table 2), the appearance of slight wrinkles in the outer surfaces of the porous structures can be appreciated, which could cause another failure mode: plastic folding. In any case, for the loads considered, the structures are still in the linear elastic region according to the stresses obtained, which proves useful for experimental planning. As will be further presented, the results agree with the experimental studies performed. Indeed, in the compression tests carried out with investment casting prototypes, linear behavior is maintained for all structures beyond the 5000 N of loading selected as the most critical case for the simulations.

4 Investment casting process evaluation

The casting technology of a magnesium alloy in ceramic molds required the solving of several issues. Firstly, it was necessary to limit the reaction of the liquid metal with the air inside the mold. The flowing metal extends its surface and the MgO oxide layer covering it is torn apart, exposing the liquid metal, and accelerating the exothermic reaction. The use of a typical SF_6 shielding gas contributes to the following reaction [37]:

$$4Mg(1) + 2O_2 + SF_6 \rightarrow 2MgO(s) + 2MgF_2(s) + SO_2F_2 \quad (1)$$

This gas increases the wettability of MgO oxide and by capillary action the liquid metal fills the cracks in the

Table 2 Summary of the results from numerical simulation

Sample	Hex 3.5			Hex 6		
Load (N) (compression along -z)	100	1000	5000	100	1000	5000
Displacement -z direction (1xe-3 mm = microns)	0.8	8.0	44.0	1.4	14.0	70.0
Max stress (Von Mises) (MPa)	3	35	172	6	57	283
Max strain (Von Mises) (%)	0.007	0.070	0.350	0.011	0.110	0.560
Apparent compression Young's modulus (GPa)	10.86			6.82		

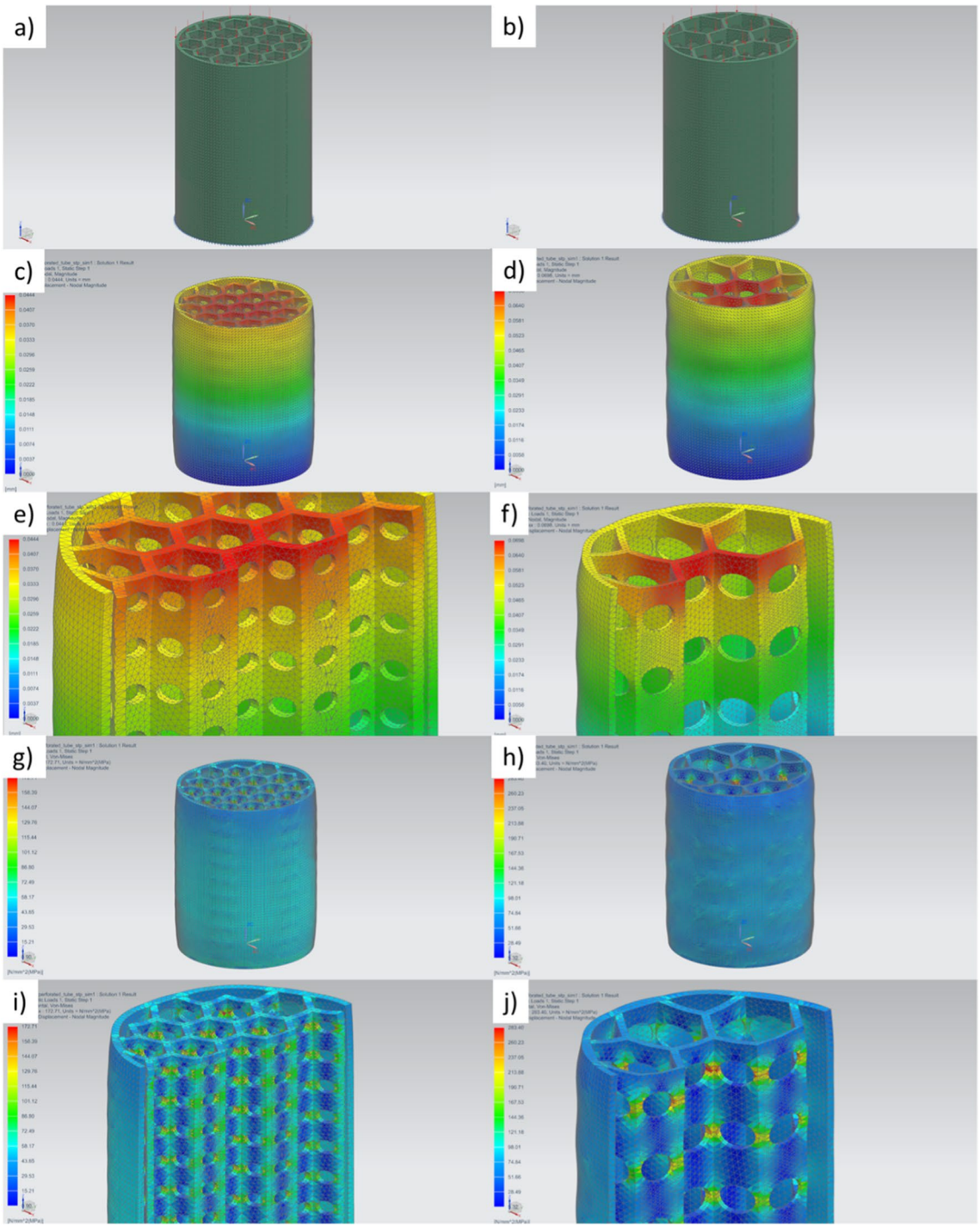

Fig. 2 Outcomes of numerical simulation: **a** direction of the load applied to HEX 3.5 structure, **b** direction of the load applied to HEX 6 structure, **c** displacement under the load of 5000 N for HEX 3.5 structure – general view, **d** displacement under the load of 5000 N for HEX 6 structure – general view, **e** displacement under the load of 5000 N for HEX 3.5 structure – cross-section, **f** displacement under the load of 5000 N for HEX 6 structure – cross-section, **g** stress under the load of 5000 N for HEX 3.5 structure – general view, **h** stress under the load of 5000 N for HEX 6 structure – general view, **i** stress under the load of 5000 N for HEX 3.5 structure – cross-section, **j** stress under the load of 5000 N for HEX 6 structure – cross-section

oxide film. The MgF_2 compound, integrated with oxides, helps to give a Pilling-Bedworth ratio close to one, thereby thickening the oxide layer and inhibiting further oxidation. To ensure a sufficient amount of gas, it was mixed with CO_2 and provided to a specially designed dome over the mold. The gas mixture was sucked into the mold cavity during the pouring and cooling phases. Any local oxidation and intense exothermic reaction can significantly increase the temperature and lead to the decomposition of the mass components in accordance with the reaction:

$$2CaSO_4 \rightarrow 2CaO + 2SO_2(g) + O_2(g) \quad (2)$$

The released oxygen will further accelerate the process, leading to an increase in gas pressure and an explosion. The first attempts showed that keeping the casting in the mold for too long also ends with the decomposition of SiO_2 from the ceramic mold and a reaction with the magnesium. The present Si atoms diffuse and usually create brittle phases of Mg_2Si (see Fig. 3), as well as places susceptible to corrosion on the surface of the casting.

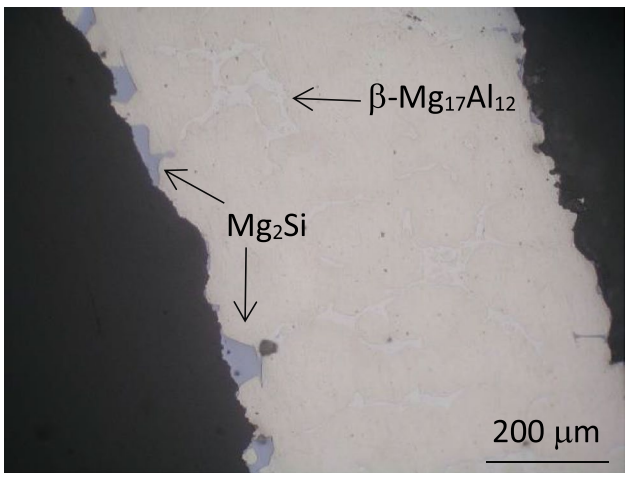

Fig. 3 Cross-section of AZ91 strut of foam with Mg_2Si formed on the surface

In terms of the Mg alloy's microstructure, if grain refinement can be obtained, the mechanical properties like compressive strength, ductility, tensile strength, hardness, yield strength could be significantly enhanced [38–40]. This effect can be assured by the usage of special alloying additives (e.g., Zr [40, 41], Zn [38, 42], Cu [43], Al [44]), particle reinforcements (e.g., CaO, ZnO [39]) or post-processing such as hot rolling [38]. Moreover, such an approach may be also beneficial for the lowering of the corrosion rate of Mg alloys [38, 40, 41]. Grain growth during casting can be also restricted by rapid cooling facilitating quick solidification and preventing the grain size increase.

Figure 4 presents subsequent stages of sample preparation for the undertaken study, starting from the model design (Fig. 4a), through 3D-printed DLP patterns (Fig. 4b) to cast element (Fig. 4c – as cast, Fig. 4d – PEO-coated, Fig. 4e – TPH-coated). In general, the quality of the replication of the polymer model in a metal part is very high. Nevertheless, mainly because of the thin-walled nature of these structures, some casting defects such as porosities localized especially on the circumference of the external envelope were noticeable. Moreover, a few transverse cracks were also observed, which may result from the rapid cooling process or damage to the mold during handling. Despite this fact, the DLP technique seems to be a proper method for the fabrication of polymer patterns for investment casting. Due to the use of a resin dedicated for casting purposes, no significant amount of ash after the burn-out cycle was stated in the mold's cavity that could interfere with a flow of the metal alloy. The previously tested FDM method can also be applicable for such structures, especially as it ensures the formation of layers creating an expanded surface area [45], but the print quality and accuracy with the use of DLP is greatly superior.

4.1 Protective coatings deposition

PEO layers were examined via SEM microscopy and presented in Fig. 5. The surface of the casting was covered with a typical PEO coating layer based on the porous network with micro-cracks and oxide granules. The flattened, so-called pancake-like features, visible in Fig. 5b, are formed

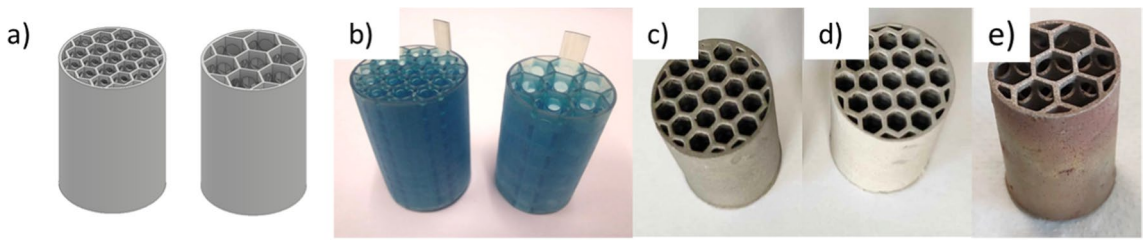

Fig. 4 Steps for the fabrication of the chosen cellular structures: **a** design (both cell sizes), **b** 3D-printed DLP patterns (both cell sizes), **c** as cast HEX 3.5, **d** PEO-coated HEX 3.5, **e** TPH-coated HEX 6

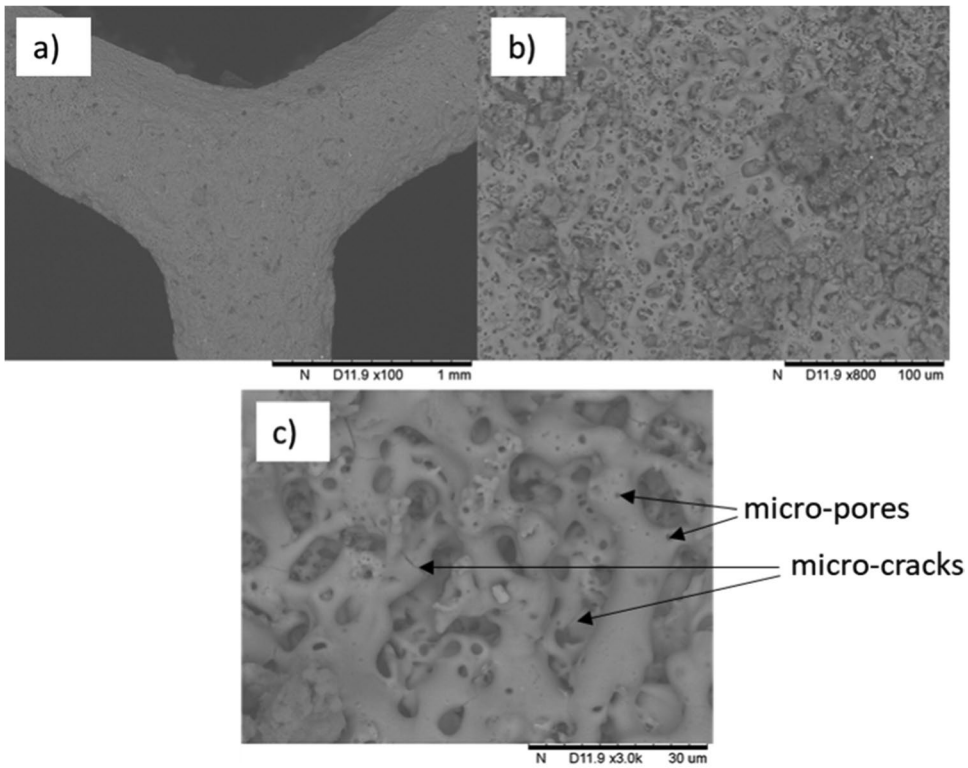

Fig. 5 SEM images of PEO-coated HEX samples: **a** 100x, **b** 800x, **c** 3000x

during the eruption of molten metal and ions accumulated in the discharge channels after relatively strong discharges. The material solidifies quickly in much cooler electrolyte producing a pancake-like morphology [39, 40, 46, 47]. The pores present on the sample surface are approx. 5–15 µm in diameter. Formation of such structures is forced by the ongoing oxidation of elements present in the alloy, and gas removal through channels during discharges [48]. These activities cause the formation of micro-pores, with a diameter of less than 5 µm, visible as a small, uniformly located dark shape in Fig. 5c [40, 41, 47, 48]. There are visible micro-cracks as well, created by a sudden solidification of the oxide layer right after molten oxide formation on the sample surface. A rapid phase change and different thermal coefficients of both the sample substrate and formed coating cause thermal stresses leading to the formation of cracks [40, 42, 43, 47, 49, 50]. A preliminary chemical composition assessment of the deposited oxide layers was performed and an exemplary result of area EDS analysis is shown in Fig. 6. Magnesium and aluminum peaks originate from the casting alloy, while the remaining sodium and phosphorus ones come from the utilized electrolyte.

Figure 7 shows FESEM images of uncoated and TPH-coated HEX porous structures. In Fig. 6c and d, it is clearly visible that tea polyphenols are deposited on the surface of AZ91 porous structure as a uniform layer of sub-micrometric spheres almost free of cracks. The morphology is similar to the one obtained in the work of Zhang et al., [51] for epigallocatechin gallate on AZ31 plane samples. The layer is more homogeneous and has less cracks compared to the one previously obtained by the author on AZ91 using tannic acid [52]. The absence of cracks in the layer is crucial to have an efficient protective effect able to modulate the degradation rate of the Mg-alloy, as recently demonstrated by the authors [53].

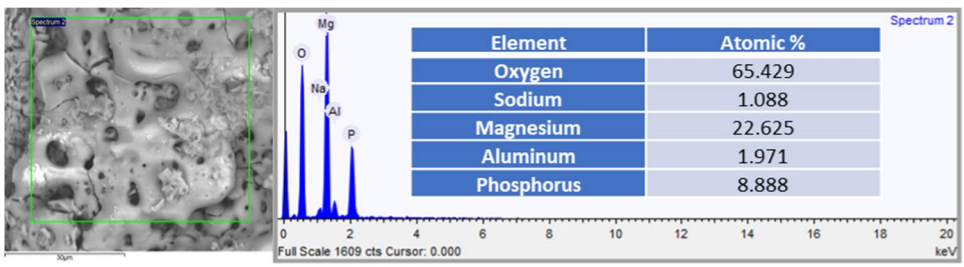

Fig. 6 Area EDS analysis of PEO-coated HEX sample

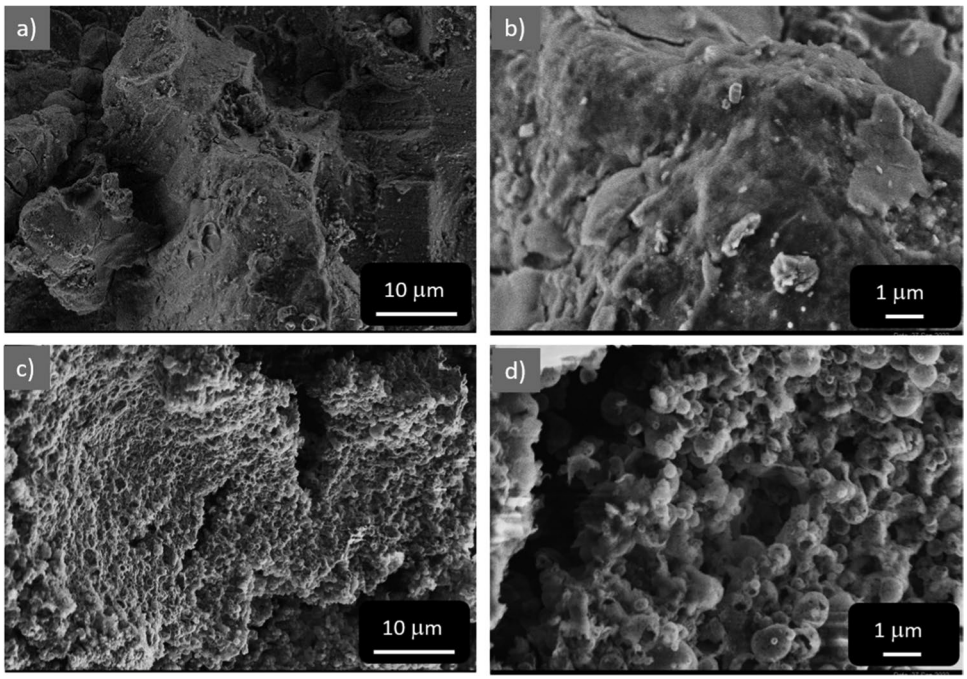

Fig. 7 FESEM images of (**a**) uncoated HEX (2000x), **b** uncoated HEX (10,000x), **c** TPH-coated HEX (2000x), **d** TPH-coated HEX (10,000x)

4.2 PBS immersion tests

Samples of uncoated and coated (PEO or TPH) castings were evaluated in terms of mass gain as a surface corrosion indicator during 6-h immersion in PBS. Base mass values equaled for the as cast, PEO-coated, and TPH-coated specimens 4.60 g, 4.65 g, and 5.96 g, respectively. Final masses after the degradation test changed accordingly to the level of 4.63 g (higher by 0.65%), 4.64 g (lower by 0.22%), and 6.25 g (higher by 4.87%). Figure 8a gathers the outcomes of mass change fraction measurements calculated after each hour of the exposure to PBS solution. After 3 h, the mass of the as cast sample has risen even more (over 1%), so the subsequent decrease probably corresponds with a detachment of corrosion products or even pieces of the casting itself. Mass gain was the most pronounced for the TPH-coated specimen, while for the PEO-coated HEX, it remained at a constant level. Additionally, pH measurements were conducted simultaneously for each of the PBS containers (see Fig. 8b). For the PEO-coated HEX pH remained at 7 for the whole time, while for both of the two remaining materials, pH started to increase drastically from the very beginning up to the range of 10–11.

Figure 9 presents the comparison photos of the set of samples taken hourly up to 6 h, while Fig. 10 shows the final macroscopic view of the surface of the as cast and TPH-coated samples after the completed test (6 h). It can be seen that PEO-coated HEX seemed to be unaffected by the PBS environment (no changes visible on the surface and constant mass), leading to the conclusion that this type of coating fulfilled its purpose, preventing the casting from untimely bioresorption of Mg. Nevertheless, it has to be considered that the PEO coating cannot be water-tight as it possesses defects such as cracks on the surface and, in

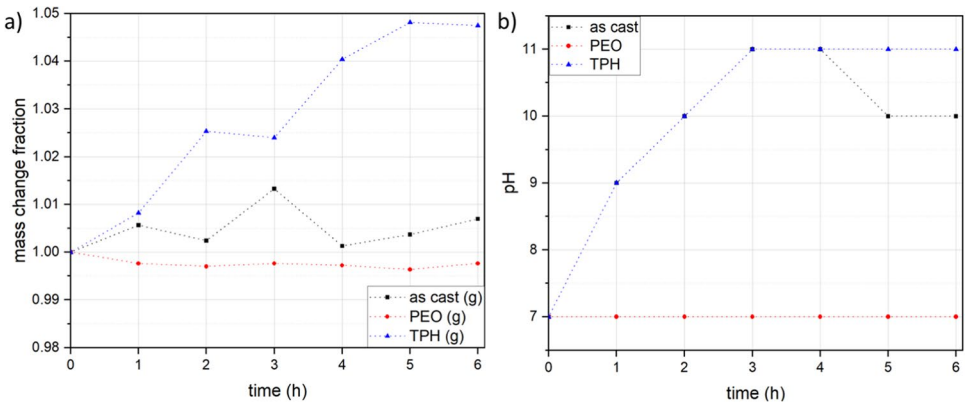

Fig. 8 Degradation test in PBS: **a** mass change fraction vs time dependence, **b** pH vs time dependence

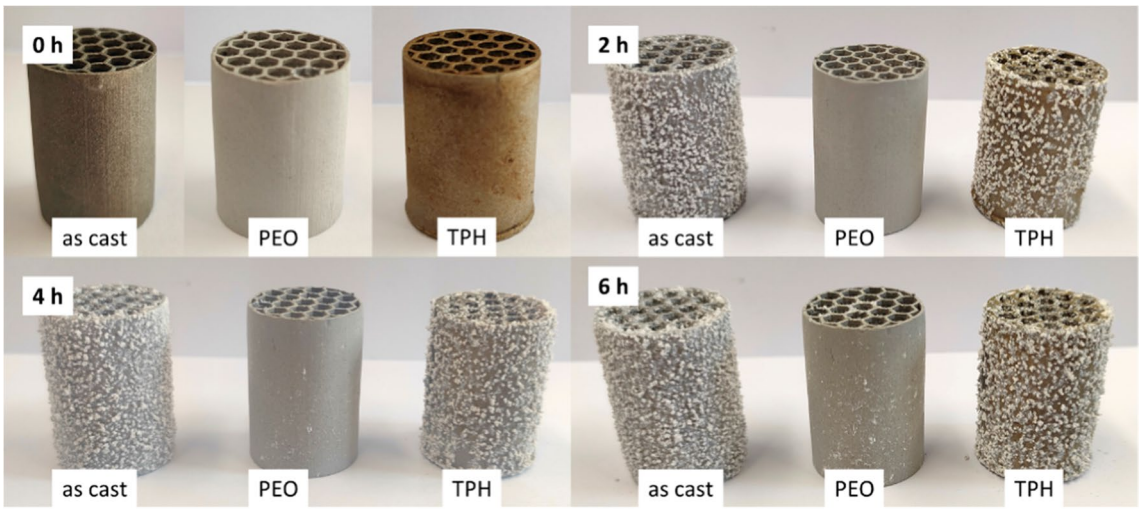

Fig. 9 View of the set of samples (as cast, PEO-coated, TPH-coated) during degradation test in PBS for 6 h

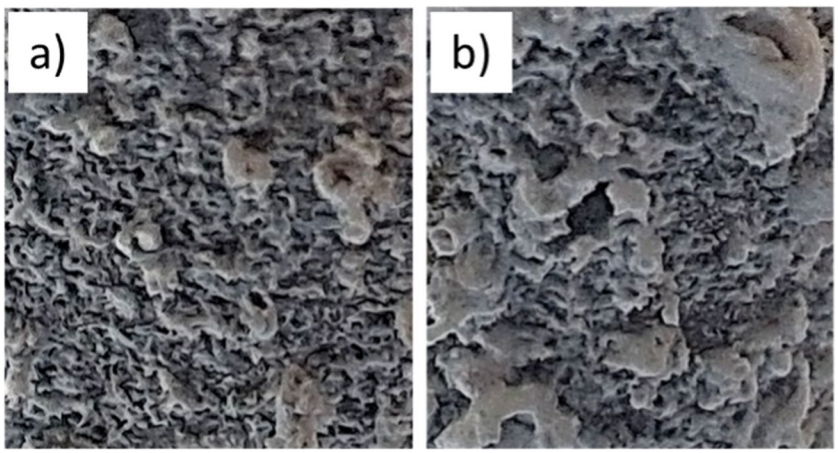

Fig. 10 Macro photographs of specimens' surfaces after degradation test in PBS: **a** as cast HEX, **b** TPH-coated HEX

case of prolonging the exposition to the PBS environment, the observed protection may deteriorate. For the as cast and TPH-coated castings, the mass change was significantly more rapid, especially for the latter one. Contrary to the preliminary assumptions, the TPH coating has not restrained the mass change, being even more susceptible than the uncoated Mg-alloy. The rapid degradation of TPH-coated samples can be ascribed to small defects in the coating through the large and complex porous structure. The possibility to combine TPH and PEO to add a sealing and biologically active layer to PEO coatings will be explored in the future. The built-up degradation layers consisted of porous white precipitates increasing in thickness along with the immersion time. Flocculent sediment on the as cast and TPH-coated HEX specimens exhibited rather pancake-like structures. Thus, corrosion products are expected to be composed of magnesium oxides and phosphate species as was also stated by the authors for AZ31 alloy in previous studies [53]. Fekry et al., [54] compared AZ31 and AZ91 alloys in terms of corrosion in PBS and found that AZ91 tends to be more resistant.

4.3 Compressive behavior

It is worth mentioning that in the preliminary stage of the study, honeycomb structures without the external tube were also considered. Nevertheless, as was proved by the first mechanical properties tests, they were evaluated as too weak for the planned application (see Fig. 11) with the maximum carried loads of 6 kN for HEX 3.5 and 2 kN for HEX 6. Reinforcing them with an additional outer pipe of the same thickness as all walls ensured the increase of loads to be withstood up to the level of over 14 kN and 8 kN, respectively, so 2.3 and 4 times. Considering the addition of the cross-section of the pipe, the increase in the active cross-section carrying the load was equal to 22.9% for HEX 3.5 and 28.3% for HEX6. Whereas the measured load transfer is much higher. These two elements, the pipe, and the hexagonal structure,

when combined, bring a significant increase in strength than they do separately. The synergistic effect is presumably due to hexagonal structure stabilization and buckling prevention. Figure 12a reveals the differences between the HEX 3.5 and HEX 6 groups, but it has to be considered that these constructs differ in the cross-section's areas – as their ratio is (3.5/6) approx. equal to 1.37. Despite this fact, it can be observed that the additional orifices inside the honeycombs act like buckling initiators, which was also pronounced in [48, 49, 55, 56]. It can be seen in Fig. 12b, that in the locations of these perforations a plastic folding process of the structure (wrinkling visible on the external wall) was initiated. Such kind of a deformation is widely evaluated as the most effective energy absorption mechanism [57].

Figures 13 and 14 present the compressive stresses vs strain calculated for both kind of the considered structures for the as cast and variously coated ones, respectively for HEX 3.5 and HEX 6. The main purpose of the chosen coatings deposition was to enable obtaining control over degradation time by lowering of the bioresorption rate and prolonging operation in body fluids strengthened with antibacterial and anti-inflammatory properties [58]. Compression tests were performed until the failure of the sample, which usually occurred in spots weakened by some casting defects (e.g., microporosity, sponginess). It can be concluded that the coating process affects the compressive performance in a consistent way, regardless of the cell diameter. In case of PEO layers, it slightly decreases the maximum compressive

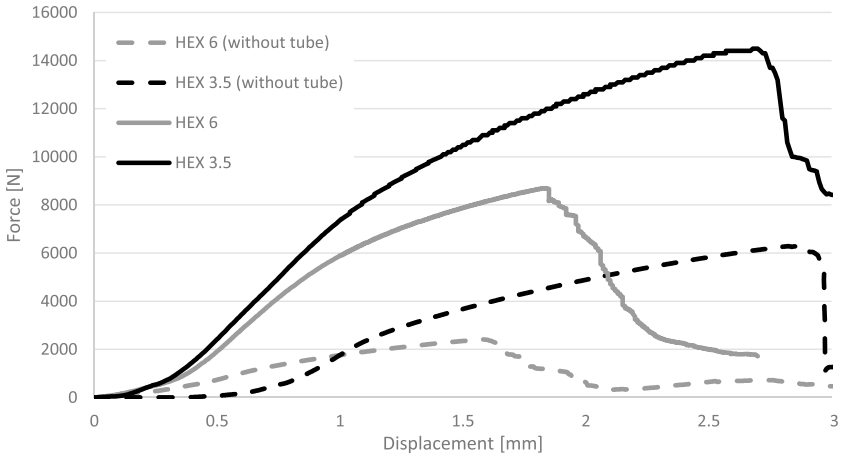

Fig. 11 Force vs displacement curves during compression of HEX 3.5 and HEX 6 with and without external tubes

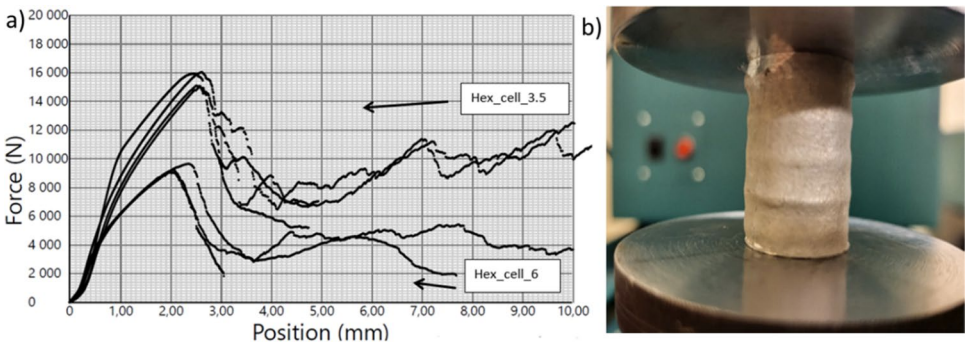

Fig. 12 Compression of AZ91 as cast structures: **a** force vs displacement dependences for HEX 3.5 and HEX 6 series of samples, **b** view of the specimen plastically folding in location of internal honeycomb perforations

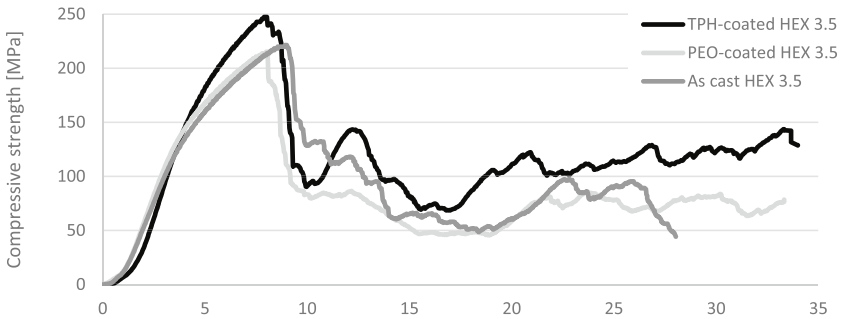

Fig. 13 Compressive strength curves for as cast and coated HEX 3.5 samples

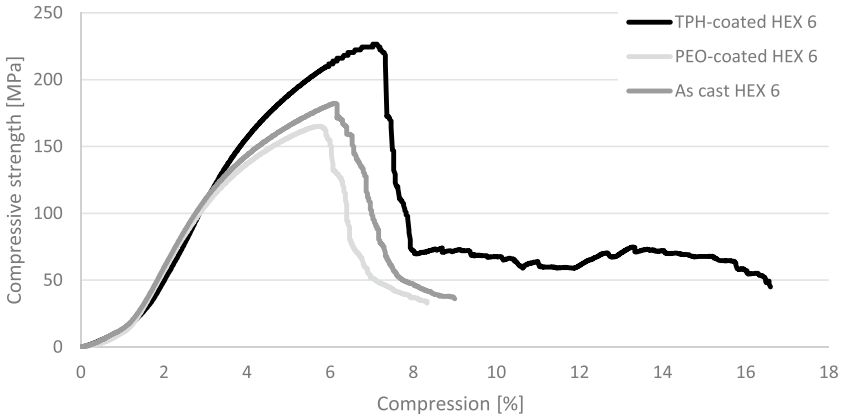

Fig. 14 Compressive strength curves for as cast and coated HEX 6 samples

strength (by 2.7%, from 221 to 215 MPa for HEX 3.5 and 9.3%, from 182 to 165 MPa for HEX 6), while organic coatings tend to reinforce these castings causing an increase in this mechanical property (by 11.8%, up to 247 MPa for HEX 3.5 and by 24.7%, up to 227 MPa for HEX 6). It can be correlated with various aspects of the process of PEO layer formation. In [59], the authors presented the compression test on AM60 alloy with a PEO layer prepared in alkaline solution, but using different duty cycles. The best results were observed for coatings formed with a duty cycle of 66%, with a minor difference to the base metal, and much lower stress was recorded for sample coated with a duty cycle of 50%. It is also worth noting, that PEO layers are formed not only on the surface of the metal, but internally as well, actually causing a slight thinning of the wall of the casting [60], while organic ones are being built externally, minimally thickening and stiffening the construct by filling the defects, simultaneously working as an obstacle for crack development and propagation [61]. An analogous effect of the mechanical property enhancement was described by Antoniac et al., [62] and Ali et al., [63] for Mg-alloys (e.g., AZ91) and calcium phosphate (CaP) layers.

Comparing the experimental results with the values of maximum stress predicted by numerical simulations, it can be stated that the structure HEX 3.5 behaved better than expected, while HEX 6 was less durable, probably by the potential occurrence of defects, which weakened the bigger cells more severely than it affected the higher amount of smaller ones where the load is distributed more efficiently. This was improved by the application of an organic coating ensuring an increase in the maximum compressive strength by over 200 MPa, being closer to the predicted level and similar to the declared works of other researchers [57, 58, 64, 65], while in [64] the elastic modulus was higher (up to 45 GPa), which is better suited for cancellous bone. Nevertheless, it has to be emphasized that the observed real test strains for maximum stresses were significantly higher (up to approx. 8%) than the ones obtained by means of numerical simulations, which can also be connected with the presence of casting imperfections and material discontinuities [66]. In fact, in terms of compressive Young's moduli, when comparing the linear regions of Figs. 9 and 10 with the simulation results from Table 2, simulations predict apparent moduli for the lattice structures of c.a. 7 to 11 GPa for the different structures, while testing results lead to values of c.a. 4 to 7 GPa. It is important to consider that simulations were performed employing a linear material with properties of reference Mg alloy (NX library), while the obtained structures behave more elastically, probably due to the mentioned casting imperfections and discontinuities. In any case, from the mechanical perspective, the values are adequate for emulating bone and related implant replacement applications. However, it should be highlighted that the evaluated structures can be adjusted in terms of the load needed to be carried by adjustment of the internal cross-section (filling), keeping the outer dimensions unchanged. Consequently, design control and complex bioinspired geometries have been demonstrated, although further exploring topology optimization strategies and their compatibility with the proposed manufacturing method is proposed to achieve enhanced biomimicry.

5 Conclusions

The manufacturing process for the creation of customized Mg-alloy structures, with tailored mechanical properties, to be used for the potential replacement of defected fragments of cortical and trabecular bones has been successfully elaborated. Investment casting utilizing DLP-printed patterns enables the fabrication of customized implants with additional perforations beneficial for tissue ingrowth, impossible to be created without the extra steps of machining with conventional techniques of plastic forming, e.g., extrusion. Comparing the proposed techniques with direct additive manufacturing, such as laser bed powder fusion, they can provide more bulk elements exhibiting a very high surface quality, without large quantity of internal

porosities, while casting defects can also occur and have to be considered. Applied protective coatings (PEO and TPH) can be effectively deposited on AZ91 substrates and can be used to postpone the degradation of implants during its presence in body fluids, also assuring the antibacterial and anti-inflammatory characteristics. In PBS degradation tests PEO-coated HEX was proved to be far more stable than the as cast and TPH-coated samples, at least considering the reported period of 6 h. The mass of the samples was higher after the test for as cast by 0.65%, for PEO 0.22% and for TPH by 4.87%. The pH grew from 7 to 10–11 for THP and as-cast specimens, while PEO sample kept pH of 7 for the whole process. The use of TPH coating associated with PEO ones with its possible sealing effect, improved the mechanical properties and the possibility to add biological functionalities to the surface (e.g., anti-inflammatory properties) can be considered as a further development. Moreover, increasing of the implant's specific surface by the application of porous PEO coating's should be beneficial for osteoblasts activity enhancing proliferation. From numerical simulation, the following conclusion was drawn. The stiffness can be modified basing on the pore size and geometry, which can allow to design the implant especially for the designated region of the bone (HEX 6 with bigger pores for trabecular bones, while HEX 3.5 with smaller pores for cortical parts). HEX 3.5 (smaller pores, higher stiffness) was characterized by negligible displacement of 44 µm under the load of 5000N, and HEX 6–70 µm. During the experimental approach, it was found out that additional coating of the samples resulted in slight change in their compressive strength. For PEO coating, HEX 3.5 get result lower by 2.7% and HEX 6 – by 9.3% in comparison to as-cast sample, while for organic coatings (TPH) the results were higher by 11.8% and 24.7%, subsequently. Overall, HEX 3.5 performed better than it was expected from numerical simulation, and HEX 6 showed lower durability, which may be connected to possible defects in the cast structure.

In future studies exploring the procedure for even more complex-shaped biomimetic geometries, the applicability to manufacturing other biomedical alloys and the biological evaluation of the achieved constructs can be considered.

Author contribution Anna Dmitruk: Conceptualization; Data curation; Investigation; Methodology; Visualization; Writing—original draft; Writing—review & editing. Andres Diaz Lantada: Data curation; Investigation; Methodology; Visualization; Writing—original draft; Writing—review & editing. Sara Ferraris: Conceptualization; Data curation; Investigation; Methodology; Visualization; Writing—original draft; Writing—review & editing. Natalia Łobacz-Raźny: Conceptualization; Data curation; Investigation; Methodology; Visualization; Writing—original draft; Writing—review & editing. Silvia Spriano: Conceptualization; Data curation; Investigation; Methodology; Visualization; Writing—original draft; Writing—review & editing. Krzysztof Naplocha: Conceptualization; Data curation; Investigation; Methodology; Supervision; Visualization; Writing—original draft; Writing—review & editing.

Funding This work has been developed in the framework of the INKplant (H2020 GA No. 953134) EU project's open-innovation cooperation "Magnesium biodegradable structures for bone implants" and under the auspices of the European Virtual Institute on Knowledge-based Multifunctional Materials AISBL (KMM-VIN).

Data availability Data will be available upon request.

Declarations

Competing interests The authors declare no competing interests.

Open Access This article is licensed under a Creative Commons Attribution 4.0 International License, which permits use, sharing, adaptation, distribution and reproduction in any medium or format, as long as you give appropriate credit to the original author(s) and the source, provide a link to the Creative Commons licence, and indicate if changes were made. The images or other third party material in this article are included in the article's Creative Commons licence, unless indicated otherwise in a credit line to the material. If material is not included in the article's Creative Commons licence and your intended use is not permitted by statutory regulation or exceeds the permitted use, you will need to obtain permission directly from the copyright holder. To view a copy of this licence, visit http://creativecommons.org/licenses/by/4.0/.

References

1. Modler N, Winkler A, Filippatos A, Weck D, Dannemann M (2020) Function-integrative lightweight engineering – design methods and applications. Chem Ing Tech 92:949–959. https://doi.org/10.1002/cite.202000010
2. Graessler I, Yang X (2019) Product life cycle cost approach for modular lightweight design. In: Procedia CIRP, Elsevier B.V., pp. 1048–1053. https://doi.org/10.1016/j.procir.2019.03.199
3. Kulkarni R (2018) Degree project mechanical engineering, second cycle, 30 credits
4. Liu T, Shi G, Li G, Wang Z (2019) Lightweight foamed concrete with foam agent addition, in: IOP Conf Ser Mater Sci Eng, Institute of Physics Publishing. https://doi.org/10.1088/1757-899X/490/3/032033
5. Xie Y, Li Z, Tang J, Li P, Chen W, Liu P, Li L, Zheng Z (2021) Microwave-assisted foaming and sintering to prepare lightweight high-strength polystyrene/carbon nanotube composite foams with an ultralow percolation threshold. J Mater Chem C Mater 9:9702–9711. https://doi.org/10.1039/D1TC01923F
6. Kramschuster A, Turng L (2010) An injection molding process for manufacturing highly porous and interconnected biodegradable polymer matrices for use as tissue engineering scaffolds. J Biomed Mater Res B Appl Biomater 92B:366–376. https://doi.org/10.1002/jbm.b.31523
7. Wan L, Huang Y, Lv S, Feng J (2015) Fabrication and interfacial characterization of aluminum foam sandwich via fluxless soldering with surface abrasion. Compos Struct 123:366–373. https://doi.org/10.1016/j.compstruct.2014.12.055
8. Feng J, Fu J, Lin Z, Shang C, Li B (2018) A review of the design methods of complex topology structures for 3D printing, Vis Comput Ind Biomed Art 1. https://doi.org/10.1186/s42492-018-0004-3

9. Plocher J, Panesar A (2019) Review on design and structural optimisation in additive manufacturing: towards next-generation lightweight structures. Mater Des 183. https://doi.org/10.1016/j.matdes.2019.108164
10. Carneiro VH, Rawson SD, Puga H, Meireles J, Withers PJ (2020) Additive manufacturing assisted investment casting: a low-cost method to fabricate periodic metallic cellular lattices. Addit Manuf 33. https://doi.org/10.1016/j.addma.2020.101085
11. Umanzor ME, Druschitz AP, Batrav, Williams CB, Reynolds WT (n.d.) Cast metal-ceramic composite lattice structures for lightweight, energy absorbing, and penetration resistant applications. http://hdl.handle.net/10919/113835
12. Braga DFO, Tavares SMO, da Silva LFM, Moreira PMGP, de Castro PMST (2014) Advanced design for lightweight structures: review and prospects. Prog Aerosp Sci 69:29–39. https://doi.org/10.1016/j.paerosci.2014.03.003
13. Orme ME, Gschweitl M, Ferrari M, Vernon R, Madera IJ, Yancey R, Mouriaux F (2017) Additive manufacturing of lightweight, optimized, metallic components suitable for space flight. In: J Spacecr Rockets, American Institute of Aeronautics and Astronautics Inc., pp. 1050–1059. https://doi.org/10.2514/1.A33749
14. Lim CWJ, Le KQ, Lu Q, Wong CH (2016) An overview of 3-D printing in manufacturing, aerospace, and automotive industries. IEEE Potentials 35:18–22. https://doi.org/10.1109/MPOT.2016.2540098
15. Tian L, Thalmann NM, Thalmann D, Zheng J (2017) The making of a 3D-printed, cable-driven, single-model, lightweight humanoid robotic hand. Front Robot AI 4. https://doi.org/10.3389/frobt.2017.00065
16. Liu CH, Chen Y, Yang SY (2022) Topology optimization and prototype of a multimaterial-like compliant finger by varying the infill density in 3D printing. Soft Robot 9:837–849. https://doi.org/10.1089/soro.2020.0212
17. Xu K, Qin S-F (2022) 3D Printing, Limb prosthetics and generative design: a scoping review. In: 2022 27th International Conference on Automation and Computing (ICAC), IEEE, pp. 1–6. https://doi.org/10.1109/ICAC55051.2022.9911138
18. Wu N, Li S, Zhang B, Wang C, Chen B, Han Q, Wang J (n.d.) The advances of topology optimization techniques in orthopedic implants: a review,. https://doi.org/10.1007/s11517-021-02361-7/Published
19. Hutmacher DW (2000) Scaffolds in tissue engineering bone and cartilage. Biomaterials 21:2529–2543. https://doi.org/10.1016/S0142-9612(00)00121-6
20. Ovsianikov A, Khademhosseini A, Mironov V (2018) The synergy of scaffold-based and scaffold-free tissue engineering strategies. Trends Biotechnol 36:348–357. https://doi.org/10.1016/j.tibtech.2018.01.005
21. Deb P, Deoghare AB, Borah A, Barua E, Das Lala S (2018) Scaffold development using biomaterials: a review. Mater Today Proc 5:12909-12919. https://doi.org/10.1016/j.matpr.2018.02.276.
22. Qu H, Fu H, Han Z, Sun Y (2019) Biomaterials for bone tissue engineering scaffolds: a review. RSC Adv 9:26252–26262. https://doi.org/10.1039/c9ra05214c
23. Uppal G, Thakur A, Chauhan A, Bala S (2022) Magnesium based implants for functional bone tissue regeneration – a review. J Magn Alloys 10:356–386. https://doi.org/10.1016/j.jma.2021.08.017
24. Liu C, Ren Z, Xu Y, Pang S, Zhao X, Zhao Y (2018) Biodegradable magnesium alloys developed as bone repair materials: a review. Scanning 2018. https://doi.org/10.1155/2018/9216314
25. Jing X, Ding Q, Wu Q, Su W, Yu K, Su Y, Ye B, Gao Q, Sun T, Guo X (2021) Magnesium-based materials in orthopaedics: material properties and animal models. Biomater Transl 2:197–213. https://doi.org/10.12336/biomatertransl.2021.03.004
26. Zhou H, Liang B, Jiang H, Deng Z, Yu K (2021) Magnesium-based biomaterials as emerging agents for bone repair and regeneration: from mechanism to application. J Magnes Alloys 9:779–804. https://doi.org/10.1016/j.jma.2021.03.004
27. Karunakaran R, Ortgies S, Tamayol A, Bobaru F, Sealy MP (2020) Additive manufacturing of magnesium alloys. Bioact Mater 5:44–54. https://doi.org/10.1016/j.bioactmat.2019.12.004
28. Sezer N, Evis Z, Koç M (2021) Additive manufacturing of biodegradable magnesium implants and scaffolds: review of the recent advances and research trends. J Magnes Alloys 9:392–415. https://doi.org/10.1016/j.jma.2020.09.014
29. Telang VS, Pemmada R, Thomas V, Ramakrishna S, Tandon P, Nanda HS (2021) Harnessing additive manufacturing for magnesium-based metallic bioimplants: recent advances and future perspectives. Curr Opin Biomed Eng 17:100264. https://doi.org/10.1016/j.cobme.2021.100264
30. Li M, Benn F, Derra T, Kröger N, Zinser M, Smeets R, Molina-Aldareguia JM, Kopp A, LLorca J (2021) Microstructure, mechanical properties, corrosion resistance and cytocompatibility of WE43 Mg alloy scaffolds fabricated by laser powder bed fusion for biomedical applications. Mater Sci Eng C 119. https://doi.org/10.1016/j.msec.2020.111623
31. Cazzola M, Corazzari I, Prenesti E, Bertone E, Vernè E, Ferraris S (2016) Bioactive glass coupling with natural polyphenols: surface modification, bioactivity and anti-oxidant ability. Appl Surf Sci 367:237–248. https://doi.org/10.1016/j.apsusc.2016.01.138
32. Cazzola M, Ferraris S, Boschetto F, Rondinella A, Marin E, Zhu W, Pezzotti G, Vernè E, Spriano S (2018) Green tea polyphenols coupled with a bioactive titanium alloy surface: in vitro characterization of osteoinductive behavior through a KUSA A1 cell study. Int J Mol Sci 19. https://doi.org/10.3390/ijms19082255
33. Rho JY, Ashman RB, Turner CH (1993) Young's modulus of trabecular and cortical bone material: ultrasonic and microtensile measurements. J Biomech 26:111–119. https://doi.org/10.1016/0021-9290(93)90042-D
34. Morgan EF, Unnikrisnan GU, Hussein AI (2018) Bone mechanical properties in healthy and diseased states. Annu Rev Biomed Eng 20:119–143. https://doi.org/10.1146/annurev-bioeng-062117-121139
35. Mirzaali MJ, Schwiedrzik JJ, Thaiwichai S, Best JP, Michler J, Zysset PK, Wolfram U (2016) Mechanical properties of cortical bone and their relationships with age, gender, composition and microindentation properties in the elderly. Bone 93:196–211. https://doi.org/10.1016/j.bone.2015.11.018
36. Ezhilmaran V, Anand PSP, Kannan S, Sivashanmugam N, Jayakrishna K, Kalusuraman G (2023) Review of bioresorbable AZ91, AZ31 and Mg–Zn–Ca implants and their manufacturing methods. Mater Sci Technol (United Kingdom) 39:901–925. https://doi.org/10.1080/02670836.2022.2153207
37. Hernandez DV, Valdes AF (2006) A kinetic study on the magnesium removal from molten aluminum using Ar-SF6-O2 gaseous mixtures. Archives of Metallurgy and Materials 51(3):433–442
38. Nayak S, Bhushan B, Jayaganthan R, Gopinath P, Agarwal RD, Lahiri D (2016) Strengthening of Mg based alloy through grain refinement for orthopaedic application. J Mech Behav Biomed Mater 59:57–70. https://doi.org/10.1016/j.jmbbm.2015.12.010
39. Ali Y, Qiu D, Jiang B, Pan F, Zhang M-X (2016) The influence of CaO addition on grain refinement of cast magnesium alloys. Scr Mater 114:103–107. https://doi.org/10.1016/j.scriptamat.2015.12.015
40. Saha P, Roy M, Datta MK, Lee B, Kumta PN (2015) Effects of grain refinement on the biocorrosion and in vitro bioactivity of magnesium. Mater Sci Eng, C 57:294–303. https://doi.org/10.1016/j.msec.2015.07.033

41. Guan S, Mei D, Wang J, Zhang Z, Du P, Bai L, Yan C, Li J, Wang J, Zhu S (2023) Mg alloy cardio-/cerebrovascular scaffolds: developments and prospects. J Magnes Alloys 11:4011–4042. https://doi.org/10.1016/j.jma.2023.09.011
42. Seyedraoufi ZS, Mirdamadi Sh (2013) Synthesis, microstructure and mechanical properties of porous Mg--Zn scaffolds. J Mech Behav Biomed Mater 21:1–8. https://doi.org/10.1016/j.jmbbm.2013.01.023
43. Antoniac I, ManescuPaltanea V, Paltanea G, Antoniac A, Nemoianu I, Petrescu M, Dura H, Bodog A (2022) Additive manufactured magnesium-based scaffolds for tissue engineering. Materials 15:8693. https://doi.org/10.3390/ma15238693
44. Wu G, Tong X, Jaing R, Ding W (2022) Grain refinement of As-cast Mg-RE alloys: research progress and future prospect. Chin Acad Sci 11. https://doi.org/10.11900/0412.1961.2021.00519
45. Dmitruk A, Naplocha K, Grzęda J, Kaczmar JW (2020) Aluminum inserts for enhancing heat transfer in PCM accumulator. Materials 13. https://doi.org/10.3390/ma13020415
46. Hussein RO, Northwood DO, Nie X (2012) The influence of pulse timing and current mode on the microstructure and corrosion behaviour of a plasma electrolytic oxidation (PEO) coated AM60B magnesium alloy. J Alloys Compd 541:41–48. https://doi.org/10.1016/j.jallcom.2012.07.003
47. Ghahfarokhi NM, Broujeny BS, Hakimizad A, Doostmohammadi A (2022) Plasma electrolytic oxidation (PEO) coating to enhance in vitro corrosion resistance of AZ91 magnesium alloy coated with polydimethylsiloxane (PDMS). Appl Phys A 128:112. https://doi.org/10.1007/s00339-021-05239-5
48. Rahmati M, Raeissi K, Toroghinejad MR, Hakimizad A, Santamaria M (2019) Effect of pulse current mode on microstructure, composition and corrosion performance of the coatings produced by plasma electrolytic oxidation on AZ31 Mg alloy. Coatings 9:688. https://doi.org/10.3390/coatings9100688
49. Aktuğ SL, Durdu S, Kutbay I, Usta M (2016) Effect of Na 2 SiO 3 ·5H 2 O concentration on microstructure and mechanical properties of plasma electrolytic oxide coatings on AZ31 Mg alloy produced by twin roll casting. Ceram Int 42:1246–1253. https://doi.org/10.1016/j.ceramint.2015.09.056
50. Liu C, Liang J, Zhou J, Li Q, Peng Z, Wang L (2016) Characterization and corrosion behavior of plasma electrolytic oxidation coated AZ91-T6 magnesium alloy. Surf Coat Technol 304:179–187. https://doi.org/10.1016/j.surfcoat.2016.07.021
51. Zhang B, Yao R, Li L, Wang Y, Luo R, Yang L, Wang Y (2019) Green tea polyphenol induced Mg^{2+} -rich multilayer conversion coating: toward enhanced corrosion resistance and promoted in situ endothelialization of AZ31 for potential cardiovascular applications. ACS Appl Mater Interfaces 11:41165–41177. https://doi.org/10.1021/acsami.9b17221
52. Spriano S, Dmitruk A, Naplocha K, Ferraris S (2023) Tannic acid coatings to control the degradation of AZ91 Mg alloy porous structures. Metals (Basel) 13:200. https://doi.org/10.3390/met13020200
53. Barberi J, Saqib M, Dmitruk A, Opitz J, Naplocha K, Beshchasna N, Spriano S, Ferraris S (2024) Characterization of tannic acid-coated AZ31 Mg alloy for biomedical application and comparison with AZ91. Materials 17:343. https://doi.org/10.3390/ma17020343
54. Fekry AM, Tammam RH (2012) Electrochemical behavior of magnesium alloys as biodegradable materials in phosphate buffer saline solution. www.electrochemsci.org
55. Murray CM, Mao M, Park J, Howard J, Wereley NM (2023) Visco-elastic honeycomb structures with increased energy absorption and shape recovery performance using buckling initiators. Polymers (Basel) 15:3350. https://doi.org/10.3390/polym15163350
56. Harvey R, Wereley N, Mao M (2020) Development of 3D printed honeycombs for crash mitigation applications. Digit Repository Univ Maryland. https://doi.org/10.13016/cooy-68mt
57. Baleh R, Abdul-Latif A, Menouer A, Razafindramary D (2018) New experimental investigation of non-conventional dynamic biaxial plastic buckling of square aluminum tubular structures. Int J Impact Eng 122:333–345. https://doi.org/10.1016/j.ijimpeng.2018.09.002
58. Gamna F, Yamaguchi S, Cochis A, Ferraris S, Kumar A, Rimondini L, Spriano S (2023) Conferring antioxidant activity to an antibacterial and bioactive titanium surface through the grafting of a natural extract. Nanomaterials 13. https://doi.org/10.3390/nano13030479
59. Alateyah AI, Aljohani TA, Alawad MO, Elkatatny S, El-Garaihy WH (2021) Improving the corrosion behavior of biodegradable AM60 alloy through plasma electrolytic oxidation. Metals 11(6):953. https://doi.org/10.3390/met11060953, https://www.mdpi.com/2075-4701/11/6/953
60. Sikdar S, Menezes PV, Maccione R, Jacob T, Mnezes PL (2021) Plasma electrolytic oxidation (PEO) process—processing, properties, and applications. Nanomaterials 11:1375. https://doi.org/10.3390/nano11061375
61. Sesia R, Spriano S, Sangermano M, Ferraris S (2023) Natural polyphenols and the corrosion protection of steel: recent advances and future perspectives for green and promising strategies, Metals (Basel) 13. https://doi.org/10.3390/met13061070
62. Antoniac I, Manescu V, Antoniac A, Paltanea G (2023) Magnesium-based alloys with adapted interfaces for bone implants and tissue engineering. Regen Biomater 10. https://doi.org/10.1093/rb/rbad095
63. Ali A, Ikram F, Iqbal F, Fatima H, Mehmood A, Kolawole MY, Chaudhry AA, Siddiqi SA, Rehman IU (2021) Improving the in vitro degradation, mechanical and biological properties of AZ91–3Ca Mg alloy via hydrothermal calcium phosphate coatings. Front Mater 8. https://doi.org/10.3389/fmats.2021.715104
64. Razavi M, Fathi M, Savabi O, Tayebi L, Vashaee D (2020) Biodegradable magnesium bone implants coated with a novel bioceramic nanocomposite. Materials 13. https://doi.org/10.3390/ma13061315
65. Razavi M, Fathi M, Savabi O, Tayebi L, Vashaee D (2018) Improvement of in vitro behavior of an Mg alloy using a nanostructured composite bioceramic coating. J Mater Sci Mater Med 29. https://doi.org/10.1007/s10856-018-6170-1
66. Wang X-S (2011) Fatigue cracking behaviors and influence factors of cast magnesium alloys. In: Special Issues on Magnesium Alloys, InTech. https://doi.org/10.5772/19075

Publisher's Note Springer Nature remains neutral with regard to jurisdictional claims in published maps and institutional affiliations.